Metabolic plasticity of sphingolipids governs cancer cell fitness in acidic tumor ecosystems

Raafat Chalar[1#], Naheel Khatri[1,2#], Jowana Obeid[1,33#], Emma Downey[1,3#], Joon-Hyun Song[1,2,4], Yujie Xiao[1,2], Andrew Chen[1], Andrew Resnick[1], Khadijeh Karbalaei[1], Janet J. Allopenna[1], Cungui Mao[1], Christopher Clarke[1], Fabiola Velazquez[6], Daniel Canal[6], Yusuf Hannun[6], Mehdi Damaghi[1,2,6,7]*

1- Stony Brook Cancer Center, Stony Brook Medicine, Stony Brook University, Stony Brook, NY, USA
2- Department of Biomedical Informatics, Stony Brook University, Stony Brook, NY, 11794, USA
3- Department of Molecular Cell Biology, Stony Brook University, Stony Brook, NY, 11794, USA
4- Department of Applied Mathematics and Statistics, Stony Brook University, Stony Brook, NY, USA
5- Department of Medicine, Stony Brook University, Stony Brook, NY, 11794, USA
6- Department of Radiation oncology, Stony Brook University, Stony Brook, NY, 11794, USA
7- Department of Pathology, Stony Brook Medicine, Stony Brook University, Stony Brook, NY, 11794, USA

*** Correspondence to: Mehdi Damaghi: mehdi.damaghi@stonybrookmedicine.edu**

Abstract:

Cancer cells must adapt to harsh tumor microenvironments, including acidic stress, to survive and thrive. Understanding how cancer cells achieve this adaptation can uncover new biomarkers and therapeutic strategies. In this study, we investigated the spatial metabolic phenotypic heterogeneity of breast cancer cells in acidic habitats using spatial multi-omics approaches on 3D spheroids. We found cancer cells dynamically regulate sphingolipid metabolism to fine-tune their cell state to cope with acidic selection pressures. Cancer cells evolve mechanisms to deal with initially accumulating toxic ceramides but later adapt to it by rerouting SL metabolic pathways to eliminate them. Using advanced MALDI image analysis, and SL inhibitors on patient derived organoids, we demonstrated that cancer cells can switch between metabolic routes when key pathways are blocked, showcasing remarkable cell state plasticity. These insights highlight the potential to target metabolic plasticity as a novel therapeutic strategy to disrupt cancer adaptation and evolution, offering new avenues for cancer treatment.

Key words: Tumor ecology and evolution, Lipid phenotype, Acidic tumor microenvironment, Metabolic reprogramming, Sphingolipid signaling, Spatial phenotyping, Lipidomic, MALDI mass spectrometry

Introduction:

Cell state plasticity, a major contributor of phenotypic plasticity, is a non-genetic mechanism diverging from traditional Darwinian principles of evolution that enables cancer cells to acclimate and adapt to variations in the tumor microenvironment (TME) (*1–4*). Unlike the long process of adaptation by genetic mutations, cell state plasticity allows cancer cells to rapidly and reversibly adjust their phenotype under variable stressors (*2*, *5–8*). Phenotypic plasticity is the ability of a single genotype to produce different phenotypes in response to environmental changes. It allows cells to sense and adapt to stressors such as nutrient deprivation, hypoxia, or acidosis without requiring genetic alterations. One hallmark of cellular adaptability is metabolic plasticity, wherein cells reprogram their metabolic pathways to maintain energy balance and survival, such as in glucose metabolism towards glycolysis or oxidative phosphorylation in the absence or presence of oxygen, respectively (*5*). In this study, we discovered ceramide metabolic plasticity as a signature feature to acidosis stress, enabling cells to redirect sphingolipid metabolism and preserve homeostasis under harsh microenvironmental conditions. Such plastic responses shape evolution by influencing which traits are exposed to selection and can, over time, become genetically stabilized, thereby enhancing evolvability and adaptive diversification.

The early-stage breast TME is heterogeneous in nature, as cells inhabit a spectrum of conditions characterized by fluctuating oxygen, pH, and nutrient availability (*5*, *9*). In ductal carcinoma in situ (DCIS), as oxygen levels decrease towards the center of a duct, cells switch their metabolism from oxidative phosphorylation to glycolysis, leading to the accumulation of lactic acid, causing acidosis (*10*). Acidosis is not solely found in hypoxic regions; indeed, several studies have shown that cancer cells remain predominantly glycolytic even in the presence of oxygen, a phenotype called " Warburg effect"(*5*, *11*). Consequently, the lack of perfusion in regions such as the center of ducts in ductal carcinoma creates the acidic habitat.

To date, lipids are rather underexplored in cancer evolution and are emerging as multifaceted players, exerting profound influences on cellular fate through their roles as energy reservoirs, structural building blocks, and critical signaling molecules (*12–14*). Lipids are active participants in crucial signaling pathways that can define cell state, fitness, and fate (*15*). They contribute to apoptosis and cell survival pathways, with specific sphingolipids (SLs) acting as signaling molecules in programmed cell death, cellular proliferation, and angiogenesis (*16*). SLs are an interconnected web of bioactive lipids influential in a plethora of cellular signaling functions (*13*, *17*). The dynamic balance between different SL species provides cancer cells with the flexibility to switch between survival and death pathways, a hallmark of their plasticity.

While acidosis is known to shape metabolic rewiring in cancer cells (*7*, *18*, *19*), key gaps remain in our understanding of how spatially distinct metabolic processes drive cancer cell adaptation and evolution in acidic niches. Moreover, despite the growing recognition of metabolomics as a powerful tool to investigate tumor biology, there is a scarcity of spatial metabolomics studies that integrate metabolic profiles with evolutionary approaches, limiting our ability to fully delineate how local microenvironmental conditions shape tumor cell states. To understand the dynamic and ecological distribution of SLs in acidic habitats and their possible role in adaptation to acidosis, we designed a spatial multi-omics approach in MCF7 breast cancer 3D spheroids using Matrix-Assisted Laser Desorption Ionization (MALDI) mass spectrometry imaging and immunofluorescence (IF) multiplexing. We posit an ecological approach in cancer biology that considers the tumor as a dynamic ecosystem, incorporating both physical factors (such as acidity and hypoxia) and non-physical factors (such as cellular interactions) as essential for understanding the tumor evolution (*20*).

We have recently shown that ecological approaches can be used to study tumor habitats and cancer cell niches, leading to novel biomarker discoveries (*7, 21*). Unlike traditional methods that often focus solely on proteomic and/or transcriptomic properties of cancer cells, here we designed our multi-omics spatial approach to capture

key attributes of the TME, particularly its metabolic and lipid landscape. By mapping the spatial distribution of metabolites and lipids, we aim to highlight how these biochemical factors shape tumor cell behavior and adaptation within their habitat. This tumor ecosystem profiling revealed distinct habitat patterns, with SL and Ceramides (Cers) predominantly localized in acidic niches profiled by multiplexed-IF (mIF). Thereafter, we employed a mass spectrometry-based lipidomics approach to validate the sphingolipid dynamics of MCF7 cells in response to acute (48 hours in pH 6.5) and chronic acidosis (3 months in pH 6.5) compared to physiological pH (pH 7.4). LC/MS results showed an accumulation of several Cer species in response to acute acidosis that were reduced back to normal level under chronic acidosis. This confirmed the localized accumulation of Cers in the acidic cores of non-adapted (NA) spheroids, an enrichment that was absent in acid-adapted (AA) spheroids, corroborating our 2D mass spectrometry findings. We next inhibited each of the four major metabolic pathways responsible for Cer clearance, individually and in various combinations, in both 2D and 3D models. Blocking any single pathway, or partial combinations, did not significantly reduce cellular fitness. However, simultaneous inhibition of all clearance routes resulted in extensive cell death. These results led us to hypothesize that SL metabolic plasticity enables cells to switch metabolic states, with Cer metabolism exhibiting high malleability through compensatory cooperation among multiple pathways, making inhibition of any single route insufficient to compromise viability. To test this, we used several SL enzyme inhibitors to block the major Cer turnover pathways in 3D culture and performed MALDI imaging mass spectrometry followed by advanced computational ecological analysis. This revealed dynamic rewiring of SL metabolic routes whenever one pathway was blocked, confirming the presence of metabolic plasticity. Furthermore, we validated these findings in patient-derived breast cancer organoids, which displayed similar adaptive SL metabolic plasticity under acidic stress. Finally, by systematically combining and alternating inhibition across SL metabolic pathways, we quantified the fitness contribution of each route in 2D and 3D systems. This analysis produced a fitness landscape demonstrating that the fitness differences among individual pathways were relatively small. Using an SL-targeted CRISPR/Cas9 knockout library, we further measured single-gene fitness under acidic stress and found that, whereas multiple pathways contributed to fitness at physiological pH, under acidosis the only essential route was ceramide synthesis, thereby validating our model of SL metabolic plasticity.

Results

Ecosystem profiling using spatial multi-omics of 3D spheroids identifies sphingolipids in acidic habitats

Ductal carcinoma of the breast experiences localized acute and chronic acidosis in the tumor ecosystem during early carcinogenesis (**Extended figure 1a**). 3D spheroids provide a robust model to replicate the temporal and spatial variations of these acidic habitats within the tumor ecosystem (*20*). We and others have demonstrated that the knowledge of acidic habitats and niches can be predictive for cancer progression (*7*, *21*, *22*). Here we designed a novel multi-omics approach combining MALDI metabolomics/lipidomics and MACSima mIF, using a panel including acidosis markers such as CA9, LAMP2b, MCT1, and other cancer markers such as CD107b, CA IX, CA XII, GLUT1, GLUT3, Cytokeratin, MCT4, Ki67, cPARP, and HIF2a, to spatially correlate metabolic and lipid habitats and niches with established spatial profiles of acid habitats in 3D spheroids (**Figure 1a**). These 3D spheroids mimic the dynamic oxygen and acidic habitats in a simple 3D tumor ecosystem (*9*, *18*). Unlike traditional 2D cell cultures, which lack spatial organization, 3D spheroids capture the complex architecture of tumors, particularly in the early avascular stages, where gradients of hypoxia, acidity, and nutrient or hormone deprivation develop from the surface to the core (*5*, *10*). The sequential sectioning of the spheres allows for co-registration of spatial lipidomics and metabolomics data from MALDI slides with HE and mIF cell profiling, which is critical for linking untargeted omics discoveries to targeted spatial features (**Extended Figure 1c-e**).

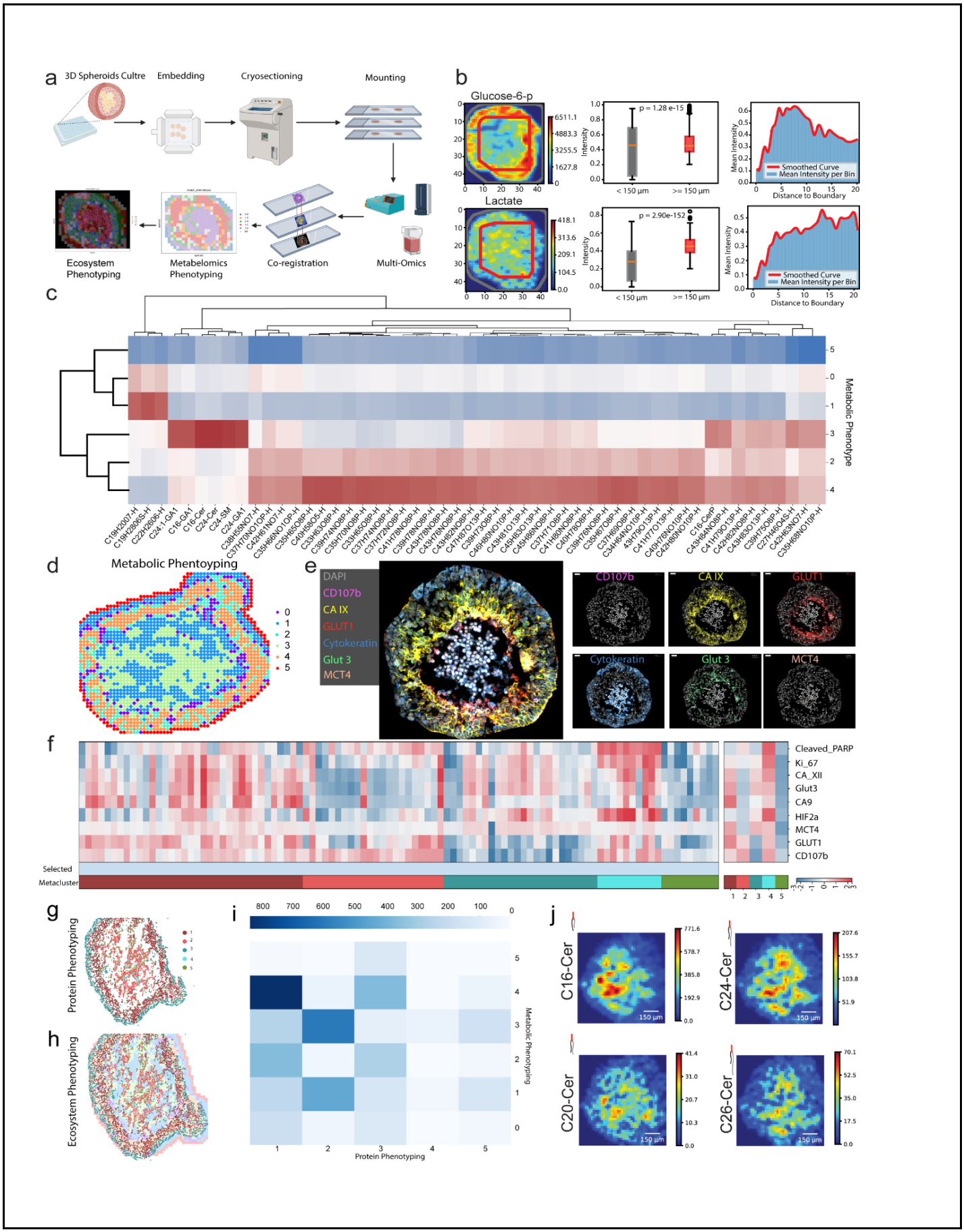
a
3D Spheroids Cultre
Embedding
Cryosectioning
Mounting
Ecosystem Phenotyping
Metabelomics Phenotyping
Co-registration
Multi-Omics
b
Glucose-6-p
p = 1.28 e-15
< 150 µm
>= 150 µm
Intensity
Mean Intensity
Smoothed Curve
Mean Intensity per Bin
Distance to Boundary
Lactate
p = 2.90e-152
c
Metabolic Phenotype
d
Metabolic Phentoyping
e
DAPI
CD107b
CA IX
GLUT1
Cytokeratin
Glut 3
MCT4
f
Cleaved_PARP
Ki_67
CA_XII
Glut3
CA9
HIF2a
MCT4
GLUT1
CD107b
Selected
Metacluster
g
Protein Phenotyping
h
Ecosystem Phenotyping
i
Metabolic Phenotyping
Protein Phenotyping
j
C16-Cer
C24-Cer
C20-Cer
C26-Cer
150 µm

Figure 1: Spatial multi-omics analysis reveals enrichment of ceramides in acidic niche. a, Schematic of the experimental workflow, including 3D spheroid culture, embedding, cryo-sectioning, and spatial multi-omics integration, including MALDI imaging, H&E staining, and multiplex mIF. **b,** Spatial intensity maps of glucose-6-phosphate (G6P) and lactate. Boxplots quantify levels in normoxic (0-150 µm from the edge) vs. hypoxic regions (>150 µm from the edge). Statistical analysis was performed using an unpaired t-test **c,** Heatmap representing the intensity of metabolites and lipids across distinct clusters normalized to scale. **d,** Unsupervised metabolic clustering visualizing spatially resolved metabolic phenotypes. **e,** Multiplex-immunofluorescence (mIF) imaging using MACSima visualizing microenvironmental markers (e.g., CD107b (LAMP2b), CA IX, Glut1, Glut3, cytokeratin) to define phenotypic niches. **f,** Single-cell resolution heatmap of mIF clusters. Scale represents normalized signal intensities. **g,** Unsupervised clustering to identify the spatial organization of the proteomic phenotypes. **h**, Ecosystem phenotyping by co-registering metabolic phenotypes and the protein phenotypes spatial clustering. **i,** Co-occurrence matrix depicting the spatial relationship between metabolic and proteomic phenotypes. Rows correspond to metabolic phenotypes; columns represent proteomic phenotypes. The color scale indicates the number of single cells from protein phenotyping clusters that are localized within the corresponding metabolic phenotyping cluster pixels. j, MALDI imaging heatmaps of various Cer species in MCF7 spheroids.

We acquired MALDI-MSI data from nine spheroid sections and detected a total of 366 ions at a 50% False Discovery Rate (FDR) threshold using METASPACE (*23*) (**Extended Figure 2a**). These included ions representing multiple adduct types, such as sodium, potassium, and chloride. From this dataset, 52 ions meeting a more stringent 10% FDR criterion were selected for downstream analysis. As a proof of principle, we first analyzed cells within habitats defined by oxygen diffusion distance, as described in our previous work (*7*). Normoxic habitats were defined as regions within 150 µm of the spheroid edge, while hypoxic habitats were located deeper within the spheroid. Abundance of known metabolites for each habitat, such as Glucose-6-P in the normoxic region and lactate concentrated in the hypoxic habitat, (**Figure 1b**), validated our habitat profiling. The selected ions were subsequently subjected to unsupervised clustering, enabling the segmentation of image pixels into distinct metabolic and lipid subtypes **(Figure 1c)**. Pixels within the same subtype exhibited similar molecular characteristics, forming distinct metabolic regions within the spheroids. Notably, these regions displayed a layered spatial organization, reflecting the gradient and heterogeneity of the tumor microenvironment (TME) (**Figure 1d, Extended Figure 2a-b**). We then found several sphingolipids (SLs), including C16-Cer, C24-Cer, sphingomyelin, and GA1, were predominantly enriched in cluster 3, localized to the central, more acidic region of the spheroids. In contrast, phospholipids such as phosphatidylserine (PS), phosphatidylethanolamine (PE), and phosphatidylcholine (PC) were enriched in cluster 4, which corresponded to the outer, proliferative layer. In parallel to MALDI, mIF was used to segment and phenotype single cells based on their marker expression profile (**Figure 1e-g, Extended Figure 2a)**. Single cells from multiple spheroids were initially clustered to group populations with similar marker expression patterns. These clusters were then subjected to meta-clustering to generate a high-level visualization of cellular phenotypes (**Figure 1f**). The identified clusters were then mapped back onto the original spheroids to reveal their spatial patterns. The two modalities were merged by co-registering the MALDI and mIF images, aligning both datasets into a common geometric space, thus enabling the calculation of a co-occurrence table linking the two types of phenotypes (**Figure 1h-i, Extended Figure 2c-e**). This analysis revealed that cells living in acidic habitats - MACSima phenotype 2, (**Figure 1f**) were mostly found in MALDI region 3, a region distinguished by enrichment in Cer and its key downstream metabolites (**Figure 1c, Extended Figure 2 and Extended Figure 3**). Sphingolipid-targeted MALDI analysis validated and extended these findings, showing elevated levels of enriched species that were identified in cluster 3 (e.g., Cer, SM, and GA1), particularly in the core of the spheroids as the most acidic zone (**Extended Figure 2d-e)**.

Ceramides are increased in response to acute acidic stress

To validate our findings, we exposed MCF7 breast cancer cells to acute acidosis (48 hours, non-adapted, NA in pH 6.5 media) (**Figure 2a**). We then employed LC/MS to quantify SLs in MCF7 cells grown in physiological pH and acidic pH (**Figure 2a**). We found several species of Cer were significantly elevated in acute acidosis (**Figure 2b**).

These observations indicated that acidosis triggers an immediate stress response marked by increased Cer levels. We then validated these findings in MCF7 spheroids to assess whether the same Cers in figure 2b accumulate to the core, characterized by hypoxia and acidosis, as compared to the normoxic and non-acidic edges (**Figure 2c**), similar

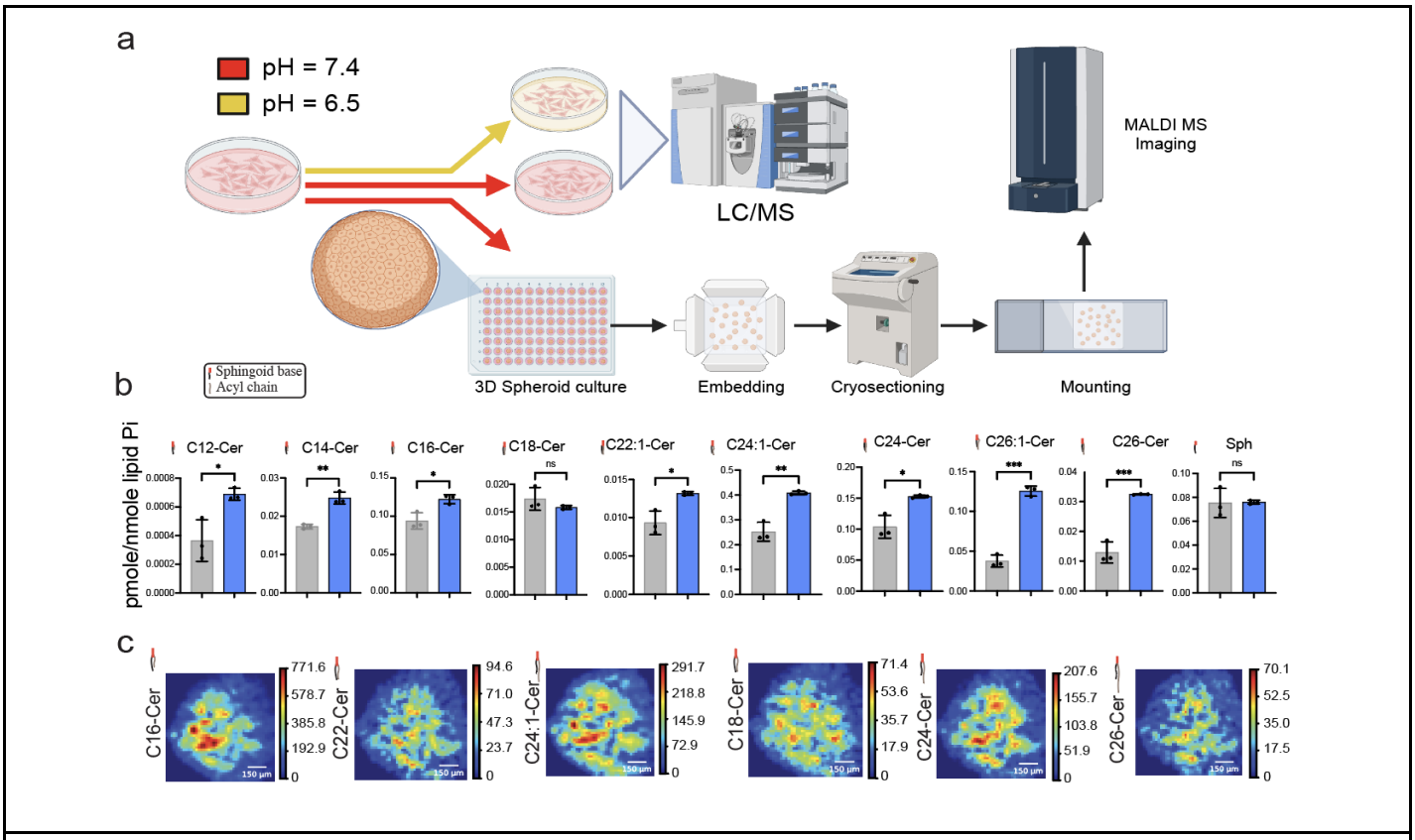

Figure 2. Sphingolipid metabolism drives breast cancer cell response to acidic stress. **a**, experimental design to measure SLs using mass spectrometry in acid exposed MCF7 cells. MALDI imaging cross comparison of the same Ceramide in MCF7 spheroid. **b**, LC/MS of absolute values of Ceramides in MCF7 exposed to acid compared to non-treated cells. Statistical analysis was performed using an unpaired t-test (*P < 0.05, **P < 0.01, ***P < 0.001, ****P < 0.0001). **c**, MALDI imaging heatmaps of Cer molecules from MCF7 spheroids.

to what we did recently (*24*). The results demonstrated remarkable consistency with the findings from the 2D culture experiments (**Figure 2c**). This pattern was reproducible in other breast cancer cell lines such as T47D and MDA-MB-231 and interestingly reversed in non-transformed breast cell lines MCF10A (**Extended figure 4a**). We also looked at Sphingomyelins (SMs), one of the primary products of Cer metabolism, and we found them exhibiting a similar pattern to that of Cers (**Extended figure 4b)**.

CRISPR-Cas screening reveals cancer cells exploit all SL clearance path to increase fitness in acidic microenvironments

To investigate these sphingolipid metabolic phenotypes in the acidic TME, we employed a CRISPR/Cas synthetic lethality screen on MCF7 cancer cells under physiological pH and acidic pH using a library targeting only genes involved in SL metabolism (**Figure 3a**) (**Supplementary table 1**). We identified key genes critical for cell survival under acidosis (**Figure 3b**), including Alkaline Ceramidase-3 (ACER3), Alkaline Ceramidase-2 (ACER2) and Acid Ceramidase (ASAH) - enzymes responsible for converting ceramide to sphingosine - as well as Sphingosine Kinase 1 (SK1), which catalyzes the phosphorylation of Sphingosine (Sph) to produce Sphingosine-1-phosphate (S1P).

Also, COL4A3BP (encoding the CERT protein) was identified as a top hit. It was shown in other cancers that Ceramide/S1P Axis is an adaptive mechanism in acute acidic microenvironments (*25*). Therefore, we first looked at this pathway, notably Sphingosine Kinase 1 (SK1), Alkaline Ceramidase-1 (ACER1), Alkaline Ceramidase-2 (ACER2) and Alkaline Ceramidase-3 (ACER3) – all enzymes responsible for clearing Cer by converting it to sphingosine (Sph) which can be subsequently metabolized to Sphingosine-1-phosphate (S1P). Cer/S1P axis can also play a pivotal role in determining cellular fate by converting tumor-suppressing ceramides and sphingosine into S1P, a tumor-promoting molecule that activates oncogenic pathways through binding to S1PR1-5 receptors (**Figure 3c**, **Extended figure 5a)** (*26*)(*27*). Thus, we performed RT- PCR for the ceramidase enzymes (ACER1, ACER2, ACER3, and ASAH1) as well as the S1P receptors (S1PR2 and S1PR3) and found significant increased expression of these genes under acute acidosis. To assess the functional effect of the S1P path on spheroid growth, we inhibited SK1 using siRNA and specific S1P synthesis inhibitor PF-543 (PF) on cancer cells in NpH and LpH. Surprisingly, inhibiting SK1 did not affect the growth rate of spheroids **(Figure 3e)**. These unexpected results suggested that cancer cells may have switched to other pathways of ceramide clearance when the S1P path is blocked and possess some degree of metabolic plasticity, enabling them to bypass SK1 dependency. To test this hypothesis and to explore pathways beyond the Cer/S1P axis, we analyzed our RNA sequencing data with specific attention to genes involved in sphingolipid metabolism **(Figure 3f)**. Differential expression analysis using DESeq2 (*28*), comparing MCF7 cells cultured under acidic versus physiological pH revealed a significant upregulation of UGT8, a key enzyme in the glycosphingolipid (GSL) synthesis pathway. UGT8 was also identified in the CRISPR screen, although with minimal effect compared to ACERs **(Figure 3b)**. To assess the functional role of this pathway, we inhibited GSL synthesis using Eliglustat (El) alone and in combination with PF. Notably, inhibition of GSL synthesis, either alone or together with S1P pathway blockade, did not produce a significant reduction in spheroid growth **(Figure 3g)**.

So far, we targeted two major Cer clearance pathways out of four (**Figure 3d**), yet cancer cell fitness remained unaffected. This resilience led us to question the extent of metabolic plasticity in cancer cells and how dynamically they can reprogram SL metabolism to maintain their fitness despite disruptions in key clearance pathways. However, to first understand whether cancer cells survive if we block all possible Cers metabolic exit pathways, we simultaneously targeted all ceramide exit pathways together in both spheroids and breast cancer patients derived organoids (PDO) (**Figure 3i and j)**. To perform this, we included HPA-12, which targets Cer trafficking and mainly disrupts Sphingomyelin (SM) biosynthesis (*29*), and NVP-231, which targets Ceramide conversion to Ceramide-1-phosphate (C1P) (*30*). Spheroid growth experiments were conducted using MCF7 and T47D cell lines to ensure the findings were not cell-line specific (**Figure 3i and Extended Figure 5e**). We found that simultaneous inhibition of all pathways leads to cancer cell death, whereas inhibition of any single one of the four pathways is insufficient to compromise cell viability (**Figure 3i and j)**. HPA-12 showed the most potent growth suppression in both MCF7 and T47D spheroids (**Figure 3i and Extended Figure 5e**). PF and eliglustat treatments increased spheroid growth, indicating a higher fitness contribution of SM and C1P pathway in 3D model. These observations raised key questions: To what extent does each ceramide clearance pathway contribute to cancer cell fitness? And do all pathways provide equivalent fitness advantages, or do some confer a greater benefit? To address these questions, we forced cancer cells to depend on a single Cer metabolic route and assessed their fitness (**Extended Figure 5**). We measured spheroid growth using inhibitors in combinations designed to restrict cells to a single route (**Extended Figure 5a**). Our results revealed that selection for the PF or El pathway conferred the lowest fitness, whereas the SM pathway, particularly under the P+E+N combination, restored spheroid growth, confirming our previous observations. Based on these findings, we constructed a fitness landscape illustrating the relative contribution of each Cer clearance pathway to cancer cell survival (**Extended Figure 5b**).

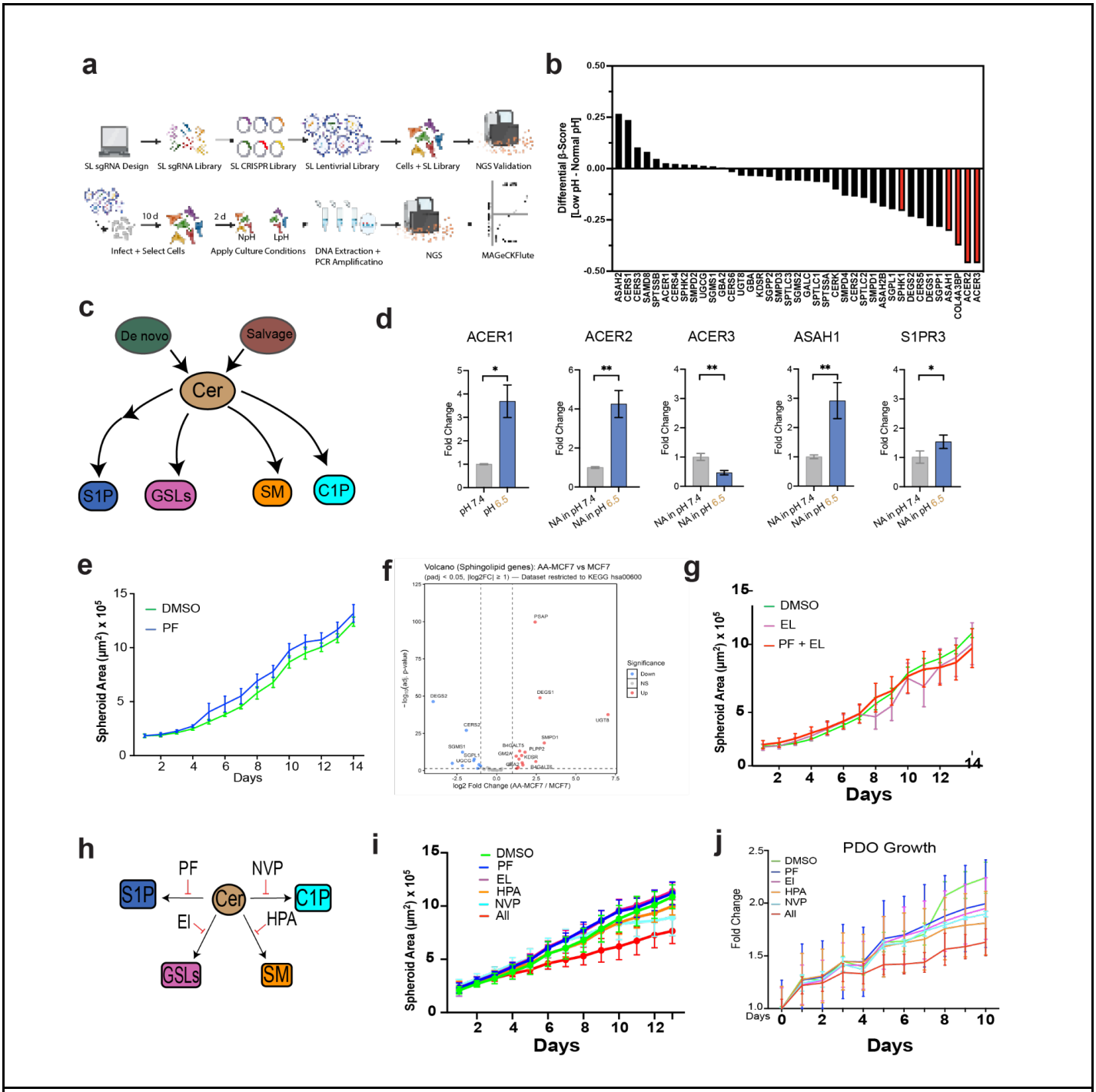

Figure 3. CRISPR screening reveals several genes from pathways of SL metabolism enhance cancer cell fitness under acute acidosis. a, Schematic representation of CRISPR/Cas9 screening targeting sphingolipid (SL) metabolism genes. **b,** Differential β-score analysis highlighting genes essential for survival under physiological pH (7.4) and acidic pH (6.5) conditions. **c,** Schematic of sphingolipid metabolism highlighting two ceramide synthesis pathways and four clearance routes. **d,** qRT-PCR analysis of genes involved in the Cer/S1P pathway, including *ACER1-3*, *ASAH1*, *S1PR2-3*, and *SGPL1*. Data are presented as fold changes. Statistical analysis was performed using an unpaired t-test (*P < 0.05, **P < 0.01, ***P < 0.001, ****P < 0.0001). **e,** Growth kinetics of MCF7 spheroids treated with SK1 inhibitor (PF) and vehicle demonstrating no difference. **f,** Volcano plot of sphingolipid metabolism–related genes differentially expressed between MCF7 cells in acid and physiological pH, highlighting coordinated transcriptional rewiring of ceramide-processing pathways. The genes set for the sphingolipid metabolism pathway was retrieved from KEGG hsa00600(*31*, *32*). Results are summarized as log2 fold changes, MCF7 under NpH and LpH, with adjusted p-values using the Benjamini-Hochberg procedure. **g,** Growth curves of MCF7 cells under pharmacologic perturbation of two sphingolipid metabolism

using PF and Eliglustat, indicating no differential sensitivity in treated spheroids even in combination of the two drugs. **h,** Model summarizing metabolic all pathways of flux away from ceramides toward pro-survival sphingolipid species. **i,** Proliferation of MCF7 spheroids treated individually and all together with inhibitors targeting distinct sphingolipid metabolic pathways, revealing pathway-specific dependencies. **j,** Longitudinal growth analysis of patient-derived tumor organoids treated with similar inhibitors in i, demonstrating conserved sensitivity to disruption of ceramide clearance in patients.

Cancer cells exhibit remarkable plasticity in regulating sphingolipid metabolism

To confirm the metabolic plasticity, we inhibited each ceramide clearance pathway in spheroids and patient derived organoids (PDOs) and performed MALDI imaging to analyze the resulting dynamics of sphingolipid metabolic pathways inhibition on other paths (**Figure 4a, Extended Figure 6, Extended Figure 7 Supplementary video 1)**. First, we evaluated the potency of the inhibitors in suppressing their respective SL products (e.g., HPA targeting SM synthesis, Eliglustat targeting GSL synthesis). Significant reductions in the target metabolic nodes were observed for each inhibitor (**Figure 4a)**. However, PF and NVP potency was not evaluated due to the low cellular levels of their targets, S1P and C1P, which were below the detection threshold in MALDI. We then applied our habitat analysis to various SL species including Cers, SMs, and GSLs (**Extended Figure 8**). Notably, we found C16-Cer levels to increase in the inner regions of spheroids treated with PF or Eliglustat, indicating that the Cer/S1P and Cer/GSL pathways are not major routes for Cer clearance and inhibiting these paths can actually accelerate the process and possibly increase the fitness. In contrast, treatment with HPA and NVP resulted in lower Cer levels in the inner and outer regions of spheroids. Eliglustat treatment effectively suppressed GSLs, as expected (**Figure 4a, Extended Figure 6 and 7**). However, spheroids treated with HPA, which inhibits the Cer/SM pathway, demonstrated a compensatory shift toward the Cer/GSL pathway. This shift was characterized by remarkably higher levels of HexCer in the outer layers of the spheroids (**Figure 4a, Extended Figure 6 and 7**). Additionally, more complex GSLs, such as C16-LacCer and C24-Gb3, displayed elevated levels in the inner regions of the spheroids under HPA treatment (**Extended Figure 6**).

SMs were also impacted by the reprogramming of SL metabolism. HPA treatment effectively reduced SM levels throughout the spheroids (**Figure 4, Extended Figure 6 and 7**). Notably, suppression of C1P synthesis with NVP-231 treatment had a significant impact on C16-SM levels, particularly in the outer layers of the spheroids (**Figure 4, Extended Figure 6 and 7**).

To visualize the spatial effects of each treatment on several SL species at once, we developed the SPHERE (Spatial Phenotype Heatmap for Ecosystem Representation) plot. These plots compare the intensity of each molecule post-treatment relative to the outer layer of DMSO controls across two spheroid regions: the outer layers (oxygen-rich, Non acidic) and the inner layers (Hypoxic, acidic) (**Figure 4b**). The SPHERE plots revealed the remarkable plasticity of sphingolipid metabolism, as shown by the distinct spatial metabolic patterns induced by each inhibitor (**Figure 4b**). Interestingly, PF and EL treatment reduced the Cers (increased their consumption) and increased SM levels implying higher fitness of SM path. HPA treatment resulted in lower ceramide levels across both regions but led to higher HexCer levels in the outer layer and increased LacCer levels in the inner region. NVP treatment showed elevated GSLs in the outer layer, along with increased SM and G6P levels. These results show that targeting specific Cer turnover pathways caused a ripple effect, reshaping the overall sphingolipid metabolic landscape across the spheroid.

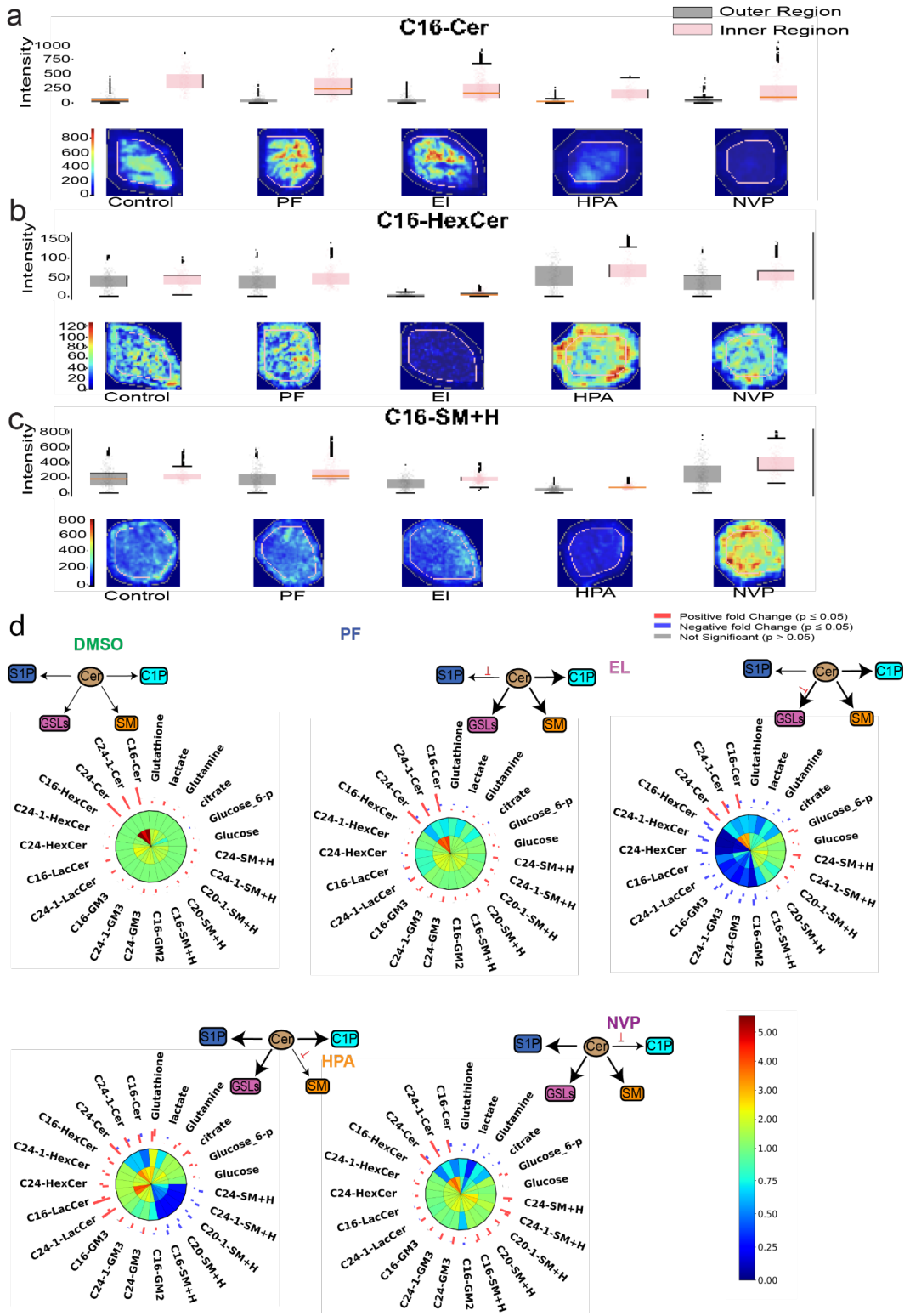

Figure 4. Spatial analysis of phenotypic plasticity and sphingolipids reprogramming in breast cancer spheroids and organoids models. **a-c,** MALDI mass spectrometry imaging (MALDI-MSI) of MCF7 spheroids treated with SL inhibitors, highlighting spatial distribution and intensity of selected molecules. Box plots indicate average molecular intensities in inner and outer layers, defined by a 125 µm threshold from the spheroid boundary. **d,** Spatial Phenotype Heatmap for Ecosystem Representation (SPHERE) plots illustrating the spatial response of various molecules to SL inhibitors. Positive and negative fold changes are indicated ($P \leq 0.05$). Schematic overlays illustrating the inferred

redistribution of ceramide flux into distinct sphingolipid pathways, including S1P, glycosphingolipids (GSLs), sphingomyelin (SM), and ceramide-1-phosphate (C1P), under selective pathway inhibition in PDOs. Collectively, these analyses demonstrate heterogeneous yet coordinated sphingolipid plasticity in patient-derived tumor organoids, supporting ceramide clearance as a conserved adaptive strategy in both complex spheroid and organoid 3D tumor ecosystems.

Ceramide clearance is maintained as a stable adaptation to chronic acidosis.

These findings indicate that ceramide clearance is broadly essential, whereas the specific metabolic route used is less critical, highlighting the substantial metabolic plasticity cancer cells employ to eliminate ceramides. Importantly, acidosis in the tumor microenvironment is not a transient stress but a chronic condition, necessitating an understanding of how prolonged acidic exposure reshapes sphingolipid metabolism and cellular adaptation. Ceramide accumulation is known to be cytotoxic and to reduce cellular fitness, raising the question of whether cancer cells merely dispose of excess ceramides or actively repurpose them to enhance fitness under stress. If ceramide clearance is adaptive rather than purely protective, prolonged acidosis would be expected to drive sustained depletion of intracellular ceramides and their redirection into pro-survival downstream metabolites, such as S1P or GSLs. To test this, MCF7 cells derived from the same parental population used in Figures 1 and 2 were adapted to pH 6.5 for more than three months (**Figure 5a**), followed by mass spectrometry analysis as described for Figure 2. Acid-adapted (AA) cells exhibited ceramide levels that were lower than NA-MCF7 cells in acid pH and even lower or comparable to those observed in physiological pH (**Figure 5b**), supporting the conclusion that sustained ceramide clearance constitutes an adaptive strategy under chronic acidic stress rewiring Cer metabolism.

We next performed MALDI imaging mass spectrometry on 3D spheroids derived from NA-MCF7 and AA-MCF7 cells. Spheroids were embedded, sectioned, and mounted on the same slide to enable simultaneous analysis and direct comparison of the spatial distribution of identical ceramide species across adaptation states. This analysis enabled pixel-by-pixel cross-comparison of ceramide abundance within equivalent microenvironmental zones of the spheroids. In NA-MCF7 spheroids, multiple ceramide species were highly enriched in the inner spheroid regions corresponding to hypoxic and acidic zones, similar to Figure 1. In contrast, AA-MCF7 spheroids exhibited a marked reduction in ceramide signal across these same regions (**Figure 5c**). Notably, the decrease was observed across nearly all detected ceramide species and was most pronounced in the spheroid core, where acidic stress is maximal. Quantification of MALDI signal intensities confirmed a significant depletion of ceramides in the acidic/hypoxic zones of AA spheroids relative to NA spheroids. These spatially resolved findings closely mirrored the reductions observed in 2D lipidomic analyses, thereby independently validating the 2D MALDI and LC/MS results within a 3D tumor ecosystem context. The marked reduction of ceramide abundance in acid-adapted spheroids suggested increased activity of ceramide clearance pathways. To examine this directly, we focused on the ceramide–sphingosine–sphingosine-1-phosphate (S1P) axis, one of the major routes of ceramide turnover. Protein-level analysis revealed increased expression of sphingosine kinase 1 (SK1) in acid-adapted cells, as confirmed by both western blotting and immunocytochemistry (ICC) (**Extended Figure 7**). ICC analysis further revealed substantial cell-to-cell heterogeneity in SK1 expression, indicating non-uniform engagement of this pathway across the population. Consistent with increased pathway activity, an in vitro SK1 activity assay demonstrated approximately a 30% increase in enzymatic activity under acute acidic conditions compared to physiological pH (**Extended Figure 7**).

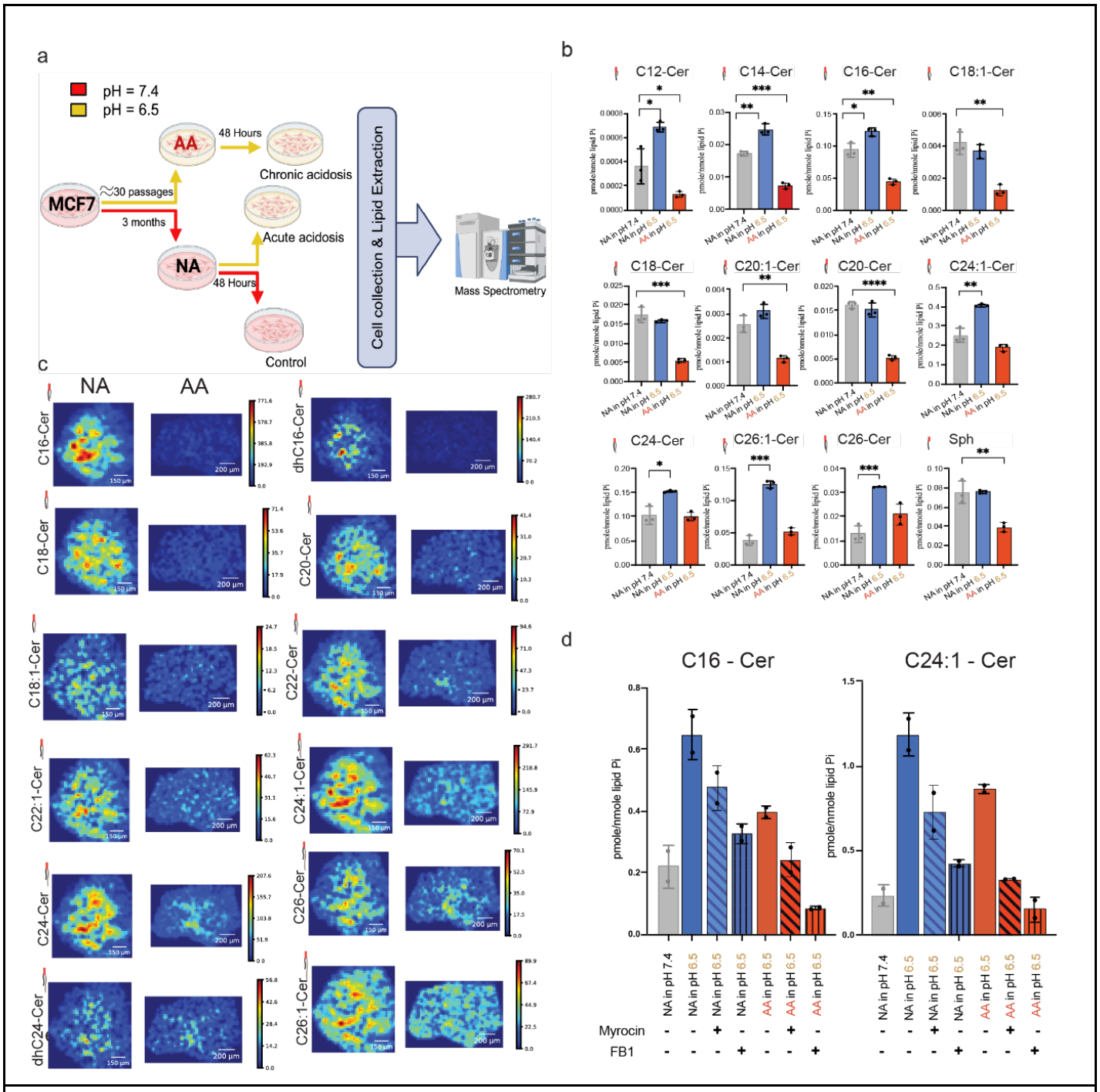

Figure 5. Chronic acidosis induces stable rewiring of ceramide metabolism and lipid spatial distribution. a, experimental design to measure SLs using mass spectrometry in acutely and chronically acid exposed MCF7 cells. Control cells were maintained at physiological pH (7.4) with the passage number matching the acid adapted cells. **b**, LC/MS of absolute values of Ceramides in MCF7 exposed to acid acutely and chronically compared to non-treated cells. **c**, MALDI imaging cross comparison of the same Ceramide in NA-MCF7 and AA-MCF7 spheroid. **d**, Mass spectrometry measurements of MCF7 cells in physiological pH and acid pH treated with Myriocin (100 nM, 48 hours) and FB1 (50 µM, 48 hours). Results are presented of the mean of two biological replicates with four technical replicates each. Statistical analysis was performed using a one-way ANOVA with multiple comparisons test. (*P < 0.05, **P < 0.01, ***P < 0.001, ****P < 0.0001, and ns p > 0.05).

Discussion:

Tumor evolution unfolds within spatially structured ecosystems in which persistent microenvironmental stressors impose strong and predictable selective pressures. Among these, extracellular acidosis is a defining feature of many solid tumors, arising early during tumorigenesis and persisting throughout progression(*33*). Survival within acidic niches therefore requires adaptive strategies that operate on ecological timescales, enabling cancer cells to maintain fitness despite chronic stress and spatial heterogeneity(*34, 35*). Our findings identify sphingolipid metabolism, specifically the regulation of ceramide turnover, as a central eco-evolutionary trait that enables cancer cell persistence in acidic tumor ecosystems.

A key insight from this work is that cancer cells do not adapt to acidosis by committing to a single optimal metabolic pathway. Instead, they exploit metabolic degeneracy, whereby multiple, biochemically distinct ceramide clearance routes converge on a shared functional outcome: avoidance of ceramide-induced cytotoxicity and preservation of growth. Degeneracy is a hallmark of robust adaptive systems and is widely observed in biological networks that must remain functional under fluctuating or unpredictable conditions(*36*). In the tumor context, this property provides resilience against both environmental stress and targeted perturbations, allowing cancer cells to maintain fitness even when individual metabolic routes are disrupted(*37*).

Our temporal analyses further reveal that adaptation to acidosis is not static. Acute acid exposure induces ceramide accumulation, consistent with ceramide's established role as a stress-responsive, pro-apoptotic lipid that reduces cellular fitness. Chronic acidosis, however, selects for phenotypes capable of mitigating this liability through sustained metabolic rewiring, resulting in reduced ceramide levels and increased flux through alternative sphingolipid pathways. This transition reflects an eco-evolutionary process in which an initially deleterious phenotype exposes variation upon which selection can act, favoring plastic responses that stabilize fitness under long-term stress. Importantly, the adaptive advantage conferred by sphingolipid plasticity appears to lie not in maximizing short-term growth, but in minimizing the risk of catastrophic failure. This aligns with principles of bet-hedging, in which organisms adopt strategies that reduce variance in fitness across time or space, even at the expense of peak performance. By maintaining access to multiple ceramide clearance routes, cancer cells effectively insure themselves against sudden environmental shifts or pathway-specific perturbations. Our observation that single-pathway inhibition rarely compromises viability, whereas simultaneous closure of all clearance routes is lethal, is consistent with selection favoring strategies that maximize long-term, or geometric mean, fitness in harsh and heterogeneous environments.

Spatial analyses further emphasize that this adaptive strategy is context dependent. Distinct sphingolipid phenotypes emerge across tumor habitats, constrained by local resource availability and stress intensity. Such spatial partitioning promotes the coexistence of multiple metabolic states within the same tumor, increasing phenotypic diversity and enhancing evolvability. This spatially maintained diversity provides a reservoir of adaptive potential that can be drawn upon during progression or therapy, offering a mechanistic explanation for the resilience of acidic tumors to metabolic intervention.

From a therapeutic perspective, these findings underscore a fundamental limitation of pathway-centric targeting strategies. In degenerate, plastic systems, inhibiting a single metabolic route is unlikely to produce durable benefit, as cells can rapidly reroute flux through alternative pathways. Instead, effective intervention may require strategies that constrain adaptive flexibility itself, by reducing network connectivity, increasing the cost of metabolic switching, or inducing evolutionary traps that exploit the liabilities of plastic states. Targeting metabolic plasticity, rather than individual pathways, may therefore represent a more effective approach to limiting tumor adaptation and evolutionary persistence.

<u>Model: sphingolipid plasticity as an adaptive fitness landscape</u>

We propose a model in which ceramide occupies a central position within an adaptive metabolic landscape shaped by acidic selection. The four major ceramide clearance routes define alternative adaptive phenotypes whose fitness values are similar in magnitude but highly interconnected. Chronic acidosis selects not only for movement away from ceramide-rich states but also for increased landscape navigability, enabling rapid transitions between routes when perturbations occur. In this landscape, fitness is maintained through redundancy and connectivity rather than optimization of a single pathway. Therapeutically, this predicts that restricting landscape connectivity, simply by

collapsing multiple escape routes or targeting the mechanisms that enable switching, may force cancer cells into low-fitness valleys, reducing adaptation and limiting evolutionary resilience.

Materials and Methods:

Cell Culture and acid adaptation

MCF-7 cells were maintained under standard culture conditions (37°C, 5% CO_2) in RPMI (Corning) supplemented with 5% FBS (Corning). Growth medium was further supplemented with 12.5 mmol PIPES, 12.5 mmol HEPES and the pH adjusted to 6.5. Cells were tested for mycoplasma contamination monthly and authenticated using short tandem repeat (STR) DNA profiling, following ATCC's guidelines. To achieve acid adaptation cells were chronically cultured and passaged upon reaching 80% confluency directly in pH 6.5 medium for approximately 3 months. Control cells or (non-adapted cells) were cultured in parallel in pH 7.4 medium to obtain a control group with the same passage number as AA cells. Acid-adapted (AA) and non-adapted (NA) cells underwent about 35 passages.

For inhibitor studies, the following compounds were used: Fumonisin B1 (50 µM, BML-SL220) as a ceramide synthase inhibitor, Myriocin (100 nM, M1177, Sigma) as an SPT inhibitor, PF-543 (100 nM, 567741, Calbiochem) as an SK1 inhibitor, Eliglustat (200 nM, M15398) as a glucosylceramide synthase inhibitor, HPA-12 (10 µM, 28350) as a CERT inhibitor, and NVP-231 (500 nM, 13858) as a ceramide kinase-1 inhibitor.

3D Spheroids processing

We grew spheroids using U-bottom 96 well plates with at least 10 replicates per condition. 2000 cells per well were seeded in a sterile, ultra-low-attachment U-bottom 96-well plate and incubated under standard culture conditions (37°C, 5% CO_2). The following day, the plate was centrifuged at 18 x g for 5 minutes at 25°C to initiate cell aggregation within each well. The plate was then incubated for an additional 2 days. After this incubation period, the medium was changed, and 5% Matrigel (356237, Corning) was added to each well. The plate was centrifuged again at 18 x g for 5 minutes at 25°C. The plates were imaged every 24 hours using Cytation 10 automated imaging, and the sectional area of the spheroids was measured to generate growth rate curves using (Software “Gen5”). On the final day, the spheroids were collected, washed in PBS, embedded in a gelatin mold and instantly frozen. Cryostat is used to cut the blocks into 4um sections for HE staining, followed by 4um sections for MACSima mIF staining, and finally 10 um sections for MALDI in negative and positive mode for both small and big molecules ranging from 100 to 1600 m/z.

Mass spectrometry based lipids measurement in cancer cells

Cells were collected by centrifugation at 800*g* for 5 min. Then, cells were washed one time in cold PBS and lysed in 2 mL of cell extraction mix (2:3 70%Isopropanol:Ethanol). To perform sphingolipid quantification, samples were spiked with the corresponding internal standards (50 pmol), and extracts were then analyzed by the Lipidomic Core Facility at Stony Brook University Medical Center, as described previously. Sphingolipid species were identified on a Thermo Finnigan TSQ700 triple quadrupole mass spectrometer. Sphingolipids from cellular extracts were normalized to total lipid phosphates present in the cells after a Bligh and Dyer extraction.

Embedding and cryo-sectioning of spheroids

Spheroids were washed with PBS and fixed in 5% PFA for 30 minutes at room temperature. They were then embedded in 10% Gelatin using a plastic mold and stored at -80 °C. Cryo-sectioning was then performed on a CM1950 cryostat (Leica Biosystems GmbH, Nussloch, Germany). Frozen blocks were mounted with carboxymethyl cellulose (CMC) on the sample holder and were kept inside the cryostat chamber (temperature set to -20 °C) for 15 mins prior to sectioning. For H&E staining, 5 µm thick sections were used right after sectioning. For MALDI-MSI analysis, spheroid sections at 10 µm thickness were cut, and were mounted on IntelliSlides (Bruker Daltonics, Bremen, Germany) while being kept frozen. During subsequent sample preparation, frozen slides were dried in a vacuum desiccator for ~30 mins. Three matrices were applied on sequential spheroid sections, including 9-Aminoacridine (9AA) (5 mg/ml in 70 % EtOH) for analyzing metabolites, 1,5-Diaminonaphthalene (DAN) (5 mg/ml in 90 % ACN) for ceramides, and 2,5-Dihydroxybenzoic acid (DHB) (40 mg/ml in 70 % MeOH and 0.1% TFA) for sphingomyelins. The matrices were sprayed using an HTX-TM5 sprayer following the methods provided by HTX

Matrix	Temp (°C)	# Passe (Count)	Conc (mg/ml)	Flow rate (ml/min	Velocity (mm/min)
9-AA	90	8	5	0.12	1200
DAN	30	8	5	0.1	1200
DHB	75	8	40	0.1	1200

Technologies, LLC, Chapel Hill, North Carolina, United States. Matrices preparation is summarized in the table below: The matrices were sprayed using an HTX-TM5 sprayer. The spraying parameters are indicated in Supplementary Table S1.

MALDI mass spectrometry imaging

MALDI-MSI experiments were performed on a timsTOFfleX mass spectrometer (Bruker Daltonik, Bremen, Germany), operated in negative ion mode for detection of ceramides/metabolites and positive ion mode for sphingomyelins. MALDI-MSI data was acquired within the mass-to-charge ratio range of 50-2000 m/z with a spatial resolution of ~20 µm, and with optimized experimental settings previously reported in reference [Chen, Chiara, and Daniel], where validation of MADLI signals for lipids were conducted on the same instrument used in this study. All the raw data was processed in SCiLS Lab (Version 2023a Pro) to generate ion images and mass spectra, which were normalized to the total ion count. The corresponding .imzML and .ibd files extracted from SCiLS Lab were imported into METASPACE and were processed for non-targeted analysis.

Targeted MALDI analysis

For the MALDI image analysis, the coregistration of the three sequential cuts for sphingomyelin (SM), ceramides (Cer), and metabolites was performed using affine transformation. This process involved aligning the bounding boxes of each cut to ensure accurate spatial correspondence across the different molecular images. Following the alignment, the colocalization score for each pair of molecules was calculated using Pearson's correlation coefficient. Pairs exhibiting a correlation score above the threshold of 0.7 were considered significant and visualized accordingly. Additionally, analysis was conducted to compare the intensity distribution of pixels in the outer layer of spheroids, defined as within 125 µms from the boundary, with that of the inner layer. A Wilcoxon rank-sum test

was applied to determine if there were significant differences between the intensity distributions of the outer and inner layers. Code for the image analysis is available at: https://github.com/sbu-damaghi-ceel/Lipid_analysis.

Non-targeted MALDI Analysis

A cloud-based platform, METASPACE was utilized for the initial processing of MALDI mass spectrometry imaging data. METASPACE performs peak picking, filtering, and annotation. Specifically, the platform imported raw MALDI imaging datasets, measured spatial chaos, spatial isotope and spectral isotope; calculated a False Discovery Rate (FDR) for each m/z annotation; enabled selection of reliable m/z features by applying a user-defined FDR threshold (10% in this analysis). The resulting high-confidence m/z list served as the basis for downstream clustering and phenotypic analysis. And the uploaded dataset is publicly accessible at https://metaspace2020.eu/project/88020884-c6d1-11ef-a046-97350f84f65a?tab=datasets.

SPHERE Plot

To compare habitats across all experimental conditions, MALDI metabolomic and lipidomic intensities were normalized relative to the normoxic habitat of the control samples treated with DMSO, where normoxic habitats were defined as 125 µms from the boundary and hypoxic habitats were defined as >125 µms from the boundary. A heatmap of the normalized intensities was plotted on a circular axis, with radial sections corresponding to distinct habitats (normoxic and hypoxic) and angular divisions representing different molecules grouped by their biochemical class (metabolites, ceramides, and sphingolipids). Each condition (e.g., DMSO control, PF, EL, HPA, NVP) was visualized in separate plots to highlight changes in spatial intensity distributions. Statistical significance between the normoxic habitat of the control samples and the habitats across all conditions was assessed using the Mann-Whitney U test. To further illustrate molecular responses, bars overlaying the heatmap depict fold changes relative to the control normoxic habitat, with bar height representing the magnitude of the fold change and color indicating directionality (red for positive, blue for negative) and statistical significance (gray for nonsignificant, $p > 0.05$).

Construction of Sphingolipid CRISPR Library

For dropout screening studies of the sphingolipid network, a pooled library of gRNAs targeting 39 core enzymes of the sphingolipid network was developed (see Supplementary table 2 for list of genes). For this, six gRNA sequences per gene as well as 30 non-targeting control gRNA sequences were obtained from the GeCKO library. These sequences were complemented by an additional 4 independent sequences per gene designed using the CHOPCHOP algorithm. Sequences were synthesized as pooled oligos and subsequently amplified and subcloned into Lenticrispr v2.0 by Gibson cloning according to the methods of Sanjana et al. (*39*). The ligation product was transformed into 25ul of electrocompetent cells, with 10 parallel reactions performed to ensure no loss of representation. Following transformation, E. coli were plated onto 245 mm x 245 mm plates (Corning) with carbenicillin selection (50 ug/ml). The next day, all colonies were scraped and combined for plasmid DNA extraction using a endotoxin free maxiprep kit from Qiagen. For validation of the library, purified plasmid was subjected to nested PCR to amplify inserts, and a second round of PCR to add sequencing primers. PCR products from four independent reactions were purified, pooled, and sequenced by Novogene. Analysis of sequences by Bowtie (allowing for up to 1bp mismatch) showed presence of 99.2% of designed gRNAs with 85% of gRNAs in a 15-fold range (from 2000 to 30000 reads).

Sphingolipid Lentiviral Generation

To generate lentiviral particles, Sphingolipid gRNA Library was co-transfected with 1.5 µg or each viral packaging plasmid (VSV-G and dVPR) in 293T cells (2000k cells per 10cm dish) using Lipofectamine 2000 according to the manufacturer's protocol. Cells were incubated overnight with the virus, media was changed after 24 hrs, and 24 hrs later 4 mL additional media was added. At 72 hours following transfection, viral media was collected, filtered (Millipore 0.45 µm PVDF), and aliquoted for storage at -80C until use.

Synthetic Lethality Screen

For the negative selection screen, 2 x 10^5 MCF7 cells were infected with Sphingolipid lentiviral supernatant to ensure MOI of ≤ 0.3 and coverage of ≥ 300 cells expressing each gRNA. Cells were selected with puromycin (1.75 µg/mL for 10 days) to ensure viral integration and depletion of gene products. Following antibiotic selection, one aliquot of (500k) cells was collected (as a day 0 control sample) and remaining cells (500k) were placed in either the normal or acidic environment. After 48 hrs, cells were collected and all cell aliquots were harvested for gDNA via Qiagen QIAamp DNA Micro Kit (56303). Following DNA extraction, the gRNA cassettes were amplified via PCR (see supplementary table 3). After pooling like samples, Illumina indexing primers were added via additional PCR (see supplementary table 4) and PCR product was purified via Qiagen Qiaquick PCR Purification Kit (28104). Purified DNA was quantified via Qubit and equimolar amounts were pooled and submitted to Novogene for sequencing (NovaSeq X Plus Series).

Sequencing and Statistical Analysis

To assess the enrichment or depletion of each gRNA and normalize data, MAGeCK-MLE (version 0.5.9.5) statistical package and MAGeCKFlute (version 2.9) were utilized respectively. Briefly, read counts of each sample were compared to the read count from the control to generate beta scores. Differential beta scores were calculated by assessing the difference between the two experimental conditions. Experiments were conducted in biological quadruplet.

Real time PCR

Total RNA from cells was extracted using an Rneasy extraction kit (Qiagen) in accordance with the manufacturer's protocol. cDNA was synthesized from 1.0 µg of RNA using Applied Biosystems High-Capacity cDNA Reverse Transcription Kit (43-688-14) according to the manufacturer's instructions. Real-time PCR analysis was performed on a QuantaStudio 7 Flex Real-Time PCR system using Applied Biosystems PowerTrack SYBR Green Master Mix (Cat# A46012). Expression levels of mRNA were measured as a ratio with β-actin, which was the normalization control. Primer sequences used in this study are stated in supplemental Table S2.

Western Blot Analysis

Acid-adapted and non-adapted MCF-7 cells were grown with the same number of passages and used for whole-protein extraction. Lysates were collected using RIPA buffer containing 1 × protease inhibitor cocktail (Cat # 11836170001; Sigma-Aldrich). Thirty micrograms of protein per sample was loaded in the polyacrylamide–SDS gels, which later were electrophoretically transferred to nitrocellulose. Membranes were incubated with primary antibodies against rabbit polyclonal SK1 (1:1000, PIPA522994, Invitrogen), b-Actin (1:10000, Cat #3700, Cell Signaling)

SK1 Activity Assay

Sphingosine kinase activity was determined by isotope specific assay. Cells were incubated with 250nM C17-Sph (Avanti Polar Lipids) in humidified incubator at 37°C with 5% CO2. After 15 minutes of incubation, cells were washed in cold PBS and scraped in 2 ml of cell extraction mixture (70% isopropanol: ethyl acetate 2:3). Samples were spiked with 50pmol of internal standard and lipid extracts analyzed by the Lipidomic Core Facility at Stony Brook University, as described previously (*40*, *41*) Lipid levels were normalized to total inorganic phosphate.

Immunofluorescence

NA-MCF7 and AA-MCF7 cancer cells were seeded in 8 well chamber slides and treated with media at pH 7.4 or pH 6.5 for 48 hours. Then media was removed and cells were rinsed with PBS, fixed in 4% paraformaldehyde for 10 mins at room temperature, and then blocked with 4% bovine serum albumin in PBS. Samples were incubated with SK1 rabbit polyclonal primary antibody (1:1,000, PIPA522994, Invitrogen) and secondary Alexa-Fluor 488 goat anti-rabbit (1:250) antibody. Coverslips were mounted using Flurosheild Mounting Medium (Abcam, Cat# NC0200574). Images were captured using Cytation10 microscope in confocal mode.

MTT assay

Cells were incubated with MTT 1 mg/mL for 2 h under standard culture conditions (37°C, 5% CO2), The medium was then carefully removed, and the cells were washed three times with PBS. Formazan crystals were dissolved by adding 400 µL of DMSO to each well, followed by incubation at room temperature on a shaker for 30 minutes. The absorbance was measured at 570 nm using a microplate reader, PF-543, Eliglustat, HPA-12, and NVP-231 on our spheroid model, inhibiting S1P, GC, SM, and C1P respectively.

Multiplex immunofluorescence (mIF) with the MACSima imaging platform

Sample preparation: Frozen embedded spheroids were cryosectioned with a CM3050 cryostat (Leica), 8 µm sections were mounted on SuperFrost Plus slides and stored in -80°c. On the day of use, the MACSwell™ Imaging frame was directly mounted onto the slide and immediately fixed with the appropriate volume of 4% PFA solution at room temperature for 10 minutes. The slide was then washed three times with MACSima Running Buffer.

For nuclear proteins, a membrane permeabilizing protocol was performed on the sample for better quality antibody binding and imaging. The sample was fixed in cold acetone for 5 minutes at room temperature. Following this, one wash with 0.1% Triton™ X-100 in PBS as well as 3-5 additional washes with MACSima Running Buffer was performed.

Immediately before running the sample in the MACSima Imaging Platform, the sample was stained with a 1:10 dilution of DAPI staining solution in the dark at room temperature for 10 minutes. Three additional washes with MACSima Running Buffer were performed, and the appropriate volume of buffer was added in accordance with the manufacturer's protocol.

Antibodies list: Antibodies were diluted in MACSima Running Buffer in accordance with the manufacturer's recommendations and/or after being optimized for the MACSima Imaging Platform. The following antibodies were used: Cytokeratin-APC (130-123-091), CAIX-AlexaFluor488 (sc-365900), ErbB2-PE (130-127-979), GLUT1-APC (130-127-114), GLUT3-FITC (sc-74399), CD107b-PE (130-118-818), beta-Catenin-APC (130-124-444), MCT4-AlexaFluor488 (sc-376140), CD324-PE (130-127-980), Vimentin-APC (130-127-018), Fibronectin-FITC (130-122-864), SPK1-FITC (NBP2-74332F), Progesterone Receptor-AlexaFluor488 (35591), Hif2a-PE (NB100-132AF594), Cleaved-PARP1-PE (130-128-159), Ki67-PE (130-119-356).

MACSima Segmentation and Normalization

Cell segmentation was performed in MACSiQ_View software with the setting of 'constrained donut' mode which uses DAPI channel for nucleus and *** channel as cytoplasmic marker to delineate the cell boundaries. Following segmentation,cell expression tables were exported, containing quantitative marker intensities for each segmented cell. These expression profiles underwent normalization on a per-slide, channel-specific basis, scaling intensities relative to the 95th percentile to mitigate slide-to-slide variability. Subsequently, a phenotyping pipeline—adapted from the Pixie(*42*)—was applied. This involved overclustering through a Self-Organizing Map(SOM) followed by consensus hierarchical clustering on the standardized (z-scored) cluster scores. The output clusters were then further refined and annotated using a graphical user interface. This systematic approach ensured that each cell was accurately and robustly phenotyped based on its multiplexed marker expression profile, facilitating robust downstream analyses of cellular heterogeneity.

Phenotyping: MACSima and MALDI

A two-step clustering module, adapted from the Pixie framework(*42*), was employed for both MALDI and MACSima data analysis. This module involves an initial overclustering stage using a Self-Organizing Map (SOM) followed by a consensus hierarchical clustering step on the standardized (z-scored) cluster scores. The two-step clustering approach serves as a robust foundation for subsequent phenotyping efforts across different datasets.

MACSima Phenotyping For MACSima phenotyping, all control spheroids were analyzed. The workflow utilized the normalized cell expression tables derived from the segmentation process, as described earlier. The acid/hypoxia-specific panel, composed of markers CAIX, CAXII, GLUT1, GLUT3, LAMP2b, MCT4, HIF2a, Cleaved PARP and Ki-47, was used to characterize the phenotypes. The two-step clustering module generated preliminary cell clusters, which were further refined and annotated using a graphical user interface within MACSima. Manual refinement was pivotal at this stage, enabling experts to incorporate biological insights and ensure accurate phenotyping based on the multiplexed marker expression profiles.

MALDI Phenotyping: For MALDI phenotyping, all pixels from the control spheroids were included, excluding small spheroids with a radius <125 micrometers. The molecule list was thresholded using METASPACE with an FDR ≤ 10%. A robust shared molecule features list, comprising 52 molecules common to all spheroids, was identified for phenotyping（**Supplementary data S1**). The same two-step clustering module was applied to this dataset, but manual refinement was kept to a minimum to maintain the analysis' objectivity and reproducibility. This data-driven approach ensured that the phenotyping remained unbiased while focusing on metabolic subtype identification.

Integration of MALDI and MACSima

The MALDI imaging and MACSima imaging were done on two sequential cuts of spheroids, to unify them into the same geometric space a manual co-registration step was done with FIJI BigDataViewer(*43*) extension. Once co-registered, each cell not only retained its MACSima-derived proteomic phenotype but was also assigned a corresponding MALDI-derived metabolomic phenotype based on its spatial overlap with defined metabolic regions. And a co-occurrence table could be computed linking MALDI-derived metabolic regions with MACSima-defined cellular phenotypes. Each entry in the co-occurrence table represents the frequency of cells with a specific proteomic phenotype residing within a particular metabolic region. This table provides insight into spatial associations between cellular functions and local metabolic environments.

Patient derived organoids culture

Primary human tissue samples were collected with informed consent from all participants, adhering to ethical and institutional guidelines. Organoid collection and processing were performed according to the protocol outlined in Sachs et al. (*47*). Tissue fragments were minced into small pieces and transferred to a 10 mL conical tube containing digestion medium. Tissue digestion was performed using adDMEM/F12+++ medium supplemented with 5 mg/mL collagenase (Cat# C213G Sigma), with samples incubated on an incubated tube rotator at 37°C for 30–60 minutes. The digestion process was monitored under a microscope, with small organoid structures visible by the end of the incubation period.

Following digestion, tissue suspensions were washed with adDMEM/F12+++ medium and centrifuged at 400 × g for 10 minutes at room temperature to pellet the cells. For samples containing a high amount of blood, the pellet was treated with red blood cell lysis buffer, incubated on ice for 5 minutes, and washed again with adDMEM/F12+++ medium to ensure purity of the epithelial components. After RBC lysis, samples were centrifuged at 50 × g for 1 minute to pellet organoids specifically, allowing separation from any remaining debris.

The resulting cell pellet was resuspended in Matrigel (356237, Corning) and plated as 20 µL droplets onto a pre-warmed 48-well plate. Plates were incubated at 37°C for 30 minutes to allow Matrigel solidification, after which 500 µL of pre-warmed organoid medium, supplemented as detailed in the supplementary table, was added to each well. The culture medium was refreshed every 2–3 days, and the plates were imaged regularly to monitor organoid formation and growth.

References:

1. R. A. Burrell, C. Swanton, Tumour heterogeneity and the evolution of polyclonal drug resistance. *Mol. Oncol.* **8**, 1095–1111 (2014).

2. C. C. Maley, A. Aktipis, T. A. Graham, A. Sottoriva, A. M. Boddy, M. Janiszewska, A. S. Silva, M. Gerlinger, Y. Yuan, K. J. Pienta, K. S. Anderson, R. Gatenby, C. Swanton, D. Posada, C.-I. Wu, J. D. Schiffman, E. S. Hwang, K. Polyak, A. R. A. Anderson, J. S. Brown, M. Greaves, D. Shibata, Classifying the evolutionary and ecological features of neoplasms. *Nat. Rev. Cancer* **17**, 605–619 (2017).

3. G. Ciriello, L. Magnani, S. J. Aitken, L. Akkari, S. Behjati, D. Hanahan, D. A. Landau, N. Lopez-Bigas, D. G. Lupiáñez, J.-C. Marine, A. Martin-Villalba, G. Natoli, A. C. Obenauf, E. Oricchio, P. Scaffidi, A. Sottoriva, A. Swarbrick, G. Tonon, S. Vanharanta, J. Zuber, Cancer evolution: A multifaceted affair. *Cancer Discov.* **14**, 36–48 (2024).

4. J.-C. Marine, S.-J. Dawson, M. A. Dawson, Non-genetic mechanisms of therapeutic resistance in cancer. *Nat. Rev. Cancer* **20**, 743–756 (2020).

5. M. Damaghi, J. West, M. Robertson-Tessi, L. Xu, M. C. Ferrall-Fairbanks, P. A. Stewart, E. Persi, B. L. Fridley, P. M. Altrock, R. A. Gatenby, P. A. Sims, A. R. A. Anderson, R. J. Gillies, The harsh microenvironment in early breast cancer selects for a Warburg phenotype. *Proc. Natl. Acad. Sci. U. S. A.* **118**, e2011342118 (2021).

6. F. J. H. Whiting, J. Househam, A.-M. Baker, A. Sottoriva, T. A. Graham, Phenotypic noise and plasticity in cancer evolution. *Trends Cell Biol.* **34**, 451–464 (2024).

7. Y. Xiao, M. Elmasry, J. D. K. Bai, A. Chen, Y. Chen, B. Jackson, J. O. Johnson, R. J. Gillies, P. Prasanna, C. Chen, M. Damaghi, Eco-evolutionary Guided Pathomic Analysis to Predict DCIS Upstaging, *bioRxiv* (2024)p. 2024.06.23.600274.

8. S. H. Strand, B. Rivero-Gutiérrez, K. E. Houlahan, J. A. Seoane, L. M. King, T. Risom, L. A. Simpson, S. Vennam, A. Khan, L. Cisneros, T. Hardman, B. Harmon, F. Couch, K. Gallagher, M. Kilgore, S. Wei, A. DeMichele, T. King, P. F. McAuliffe, J. Nangia, J. Lee, J. Tseng, A. M. Storniolo, A. M. Thompson, G. P.

Gupta, R. Burns, D. J. Veis, K. DeSchryver, C. Zhu, M. Matusiak, J. Wang, S. X. Zhu, J. Tappenden, D. Y. Ding, D. Zhang, J. Luo, S. Jiang, S. Varma, L. Anderson, C. Straub, S. Srivastava, C. Curtis, R. Tibshirani, R. M. Angelo, A. Hall, K. Owzar, K. Polyak, C. Maley, J. R. Marks, G. A. Colditz, E. S. Hwang, R. B. West, Molecular classification and biomarkers of clinical outcome in breast ductal carcinoma in situ: Analysis of TBCRC 038 and RAHBT cohorts. *Cancer Cell* **40**, 1521–1536.e7 (2022).

9. M. Damaghi, N. K. Tafreshi, M. C. Lloyd, R. Sprung, V. Estrella, J. W. Wojtkowiak, D. L. Morse, J. M. Koomen, M. M. Bui, R. A. Gatenby, R. J. Gillies, Chronic acidosis in the tumour microenvironment selects for overexpression of LAMP2 in the plasma membrane. *Nat. Commun.* **6**, 8752 (2015).

10. M. Damaghi, H. Mori, S. Byrne, L. Xu, T. Chen, J. Johnson, N. D. Gallant, A. Marusyk, A. D. Borowsky, R. J. Gillies, Collagen production and niche engineering: A novel strategy for cancer cells to survive acidosis in DCIS and evolve. *Evol. Appl.* **13**, 2689–2703 (2020).

11. E. Persi, M. Duran-Frigola, M. Damaghi, W. R. Roush, P. Aloy, J. L. Cleveland, R. J. Gillies, E. Ruppin, Systems analysis of intracellular pH vulnerabilities for cancer therapy. *Nat. Commun.* **9**, 2997 (2018).

12. E. E. Jones, S. Dworski, D. Canals, J. Casas, G. Fabrias, D. Schoenling, T. Levade, C. Denlinger, Y. A. Hannun, J. A. Medin, R. R. Drake, On-tissue localization of ceramides and other sphingolipids by MALDI mass spectrometry imaging. *Anal. Chem.* **86**, 8303–8311 (2014).

13. L. M. Obeid, C. M. Linardic, L. A. Karolak, Y. A. Hannun, Programmed cell death induced by ceramide. *Science* **259**, 1769–1771 (1993).

14. E. E. Jones, S. Dworski, M. Kamani, D. Canals, M. Wada, X. Liu, Y. A. Hannun, J. Norris, J. A. Medin, R. R. Drake, "Detection and Distribution of Sphingolipids in Tissue by FTICR MALDI-Imaging Mass Spectrometry" in *Bioactive Sphingolipids in Cancer Biology and Therapy*, Y. A. Hannun, C. Luberto, C. Mao, L. M. Obeid, Eds. (Springer International Publishing, Cham, 2015), pp. 339–358.

15. G. D'Angelo, G. La Manno, The lipotype hypothesis. *Nat. Rev. Mol. Cell Biol.* **24**, 1–2 (2023).

16. F. N. Velazquez, C. Luberto, D. Canals, Y. A. Hannun, Enzymes of sphingolipid metabolism as transducers of metabolic inputs. *Biochem. Soc. Trans.* **52**, 1795–1808 (2024).

17. S. Alsamman, S. A. Christenson, A. Yu, N. M. E. Ayad, M. S. Mooring, J. M. Segal, J. K.-H. Hu, J. R. Schaub, S. S. Ho, V. Rao, M. M. Marlow, S. M. Turner, M. Sedki, L. Pantano, S. Ghoshal, D. D. S. Ferreira, H.-Y. Ma, C. C. Duwaerts, R. Espanol-Suner, L. Wei, B. Newcomb, I. Mileva, D. Canals, Y. A. Hannun, R. T. Chung, A. N. Mattis, B. C. Fuchs, A. M. Tager, D. Yimlamai, V. M. Weaver, A. C. Mullen, D. Sheppard, J. Y. Chen, Targeting acid ceramidase inhibits YAP/TAZ signaling to reduce fibrosis in mice. *Sci. Transl. Med.* **12**, eaay8798 (2020).

18. A. R. Freischel, M. Damaghi, J. J. Cunningham, A. Ibrahim-Hashim, R. J. Gillies, R. A. Gatenby, J. S. Brown, Frequency-dependent interactions determine outcome of competition between two breast cancer cell lines. *Sci. Rep.* **11**, 4908 (2021).

19. L. Laplane, C. C. Maley, The evolutionary theory of cancer: challenges and potential solutions. *Nat. Rev. Cancer* **24**, 718–733 (2024).

20. Y. Wang, A. B. Hummon, MS imaging of multicellular tumor spheroids and organoids as an emerging tool for personalized medicine and drug discovery. *J. Biol. Chem.* **297**, 101139 (2021).

21. A. Fortunato, D. Mallo, L. Cisneros, L. M. King, A. Khan, C. Curtis, M. D. Ryser, J. Y. Lo, A. Hall, J. R. Marks, E. S. Hwang, C. C. Maley, Evolutionary Measures Show that Recurrence of DCIS is Distinct from Progression to Breast Cancer. *medRxiv*, doi: 10.1101/2024.08.15.24311949 (2024).

22. C. Zivko, T.-H. Hahm, C. Tressler, D. Brown, K. Glunde, V. Mahairaki, Mass spectrometry imaging of

organoids to improve preclinical research. *Adv. Healthc. Mater.* **13**, e2302499 (2024).

23. A. Palmer, P. Phapale, I. Chernyavsky, R. Lavigne, D. Fay, A. Tarasov, V. Kovalev, J. Fuchser, S. Nikolenko, C. Pineau, M. Becker, T. Alexandrov, FDR-controlled metabolite annotation for high-resolution imaging mass spectrometry. *Nat. Methods* **14**, 57–60 (2017).

24. Y. Xiao, M. Elmasry, J. D. K. Bai, A. Chen, Y. Chen, B. Jackson, J. O. Johnson, P. Prasanna, C. Chen, M. Damaghi, Eco-evolutionary guided pathomic analysis detects biomarkers to predict ductal carcinoma in situ upstaging. *Cancer Res.* **85**, 2537–2547 (2025).

25. M. Cortini, A. Armirotti, M. Columbaro, D. L. Longo, G. Di Pompo, E. Cannas, A. Maresca, C. Errani, A. Longhi, A. Righi, V. Carelli, N. Baldini, S. Avnet, Exploring metabolic adaptations to the acidic microenvironment of osteosarcoma cells unveils sphingosine 1-phosphate as a valuable therapeutic target. *Cancers (Basel)* **13**, 311 (2021).

26. S. Ponnusamy, M. Meyers-Needham, C. E. Senkal, S. A. Saddoughi, D. Sentelle, S. P. Selvam, A. Salas, B. Ogretmen, Sphingolipids and cancer: ceramide and sphingosine-1-phosphate in the regulation of cell death and drug resistance. *Future Oncol.* **6**, 1603–1624 (2010).

27. N. J. Pyne, S. Pyne, Sphingosine 1-phosphate and cancer. *Nat. Rev. Cancer* **10**, 489–503 (2010).

28. M. I. Love, W. Huber, S. Anders, Moderated estimation of fold change and dispersion for RNA-seq data with DESeq2. *Genome Biol.* **15**, 550 (2014).

29. S. Yasuda, H. Kitagawa, M. Ueno, H. Ishitani, M. Fukasawa, M. Nishijima, S. Kobayashi, K. Hanada, A novel inhibitor of ceramide trafficking from the endoplasmic reticulum to the site of sphingomyelin synthesis. *J. Biol. Chem.* **276**, 43994–44002 (2001).

30. C. Graf, M. Klumpp, M. Habig, P. Rovina, A. Billich, T. Baumruker, B. Oberhauser, F. Bornancin, Targeting ceramide metabolism with a potent and specific ceramide kinase inhibitor. *Mol. Pharmacol.* **74**, 925–932 (2008).

31. M. Kanehisa, S. Goto, KEGG: kyoto encyclopedia of genes and genomes. *Nucleic Acids Res.* **28**, 27–30 (2000).

32. M. Kanehisa, M. Furumichi, Y. Sato, M. Ishiguro-Watanabe, M. Tanabe, KEGG: integrating viruses and cellular organisms. *Nucleic Acids Res.* **49**, D545–D551 (2021).

33. I. Loukas, F. Simeoni, M. Milan, P. Inglese, H. Patel, R. Goldstone, P. East, S. Strohbuecker, R. Mitter, B. Talsania, W. Tang, C. D. H. Ratcliffe, E. Sahai, V. Shahrezaei, P. Scaffidi, Selective advantage of epigenetically disrupted cancer cells via phenotypic inertia. *Cancer Cell* **41**, 70–87.e14 (2023).

34. G. S. França, M. Baron, B. R. King, J. P. Bossowski, A. Bjornberg, M. Pour, A. Rao, A. S. Patel, S. Misirlioglu, D. Barkley, K. H. Tang, I. Dolgalev, D. A. Liberman, G. Avital, F. Kuperwaser, M. Chiodin, D. A. Levine, T. Papagiannakopoulos, A. Marusyk, T. Lionnet, I. Yanai, Cellular adaptation to cancer therapy along a resistance continuum. *Nature* **631**, 876–883 (2024).

35. K. Kitatani, J. Idkowiak-Baldys, Y. A. Hannun, The sphingolipid salvage pathway in ceramide metabolism and signaling. *Cell. Signal.* **20**, 1010–1018 (2008).

36. L. A. Sena, N. S. Chandel, Physiological roles of mitochondrial reactive oxygen species. *Mol. Cell* **48**, 158–167 (2012).

37. L. B. Sullivan, N. S. Chandel, Mitochondrial reactive oxygen species and cancer. *Cancer Metab.* **2**, 17 (2014).

38. D. B. Zorov, M. Juhaszova, S. J. Sollott, Mitochondrial reactive oxygen species (ROS) and ROS-induced ROS release. *Physiol. Rev.* **94**, 909–950 (2014).

39. N. E. Sanjana, O. Shalem, F. Zhang, Improved vectors and genome-wide libraries for CRISPR screening. *Nat. Methods* **11**, 783–784 (2014).

40. J. Bielawski, J. S. Pierce, J. Snider, B. Rembiesa, Z. M. Szulc, A. Bielawska, Comprehensive quantitative analysis of bioactive sphingolipids by high-performance liquid chromatography-tandem mass spectrometry. *Methods Mol. Biol.* **579**, 443–467 (2009).

41. J. Bielawski, J. S. Pierce, J. Snider, B. Rembiesa, Z. M. Szulc, A. Bielawska, Sphingolipid analysis by high performance liquid chromatography-tandem mass spectrometry (HPLC-MS/MS). *Adv. Exp. Med. Biol.* **688**, 46–59 (2010).

42. C. C. Liu, N. F. Greenwald, A. Kong, E. F. McCaffrey, K. X. Leow, D. Mrdjen, B. J. Cannon, J. L. Rumberger, S. R. Varra, M. Angelo, Robust phenotyping of highly multiplexed tissue imaging data using pixel-level clustering. *Nat. Commun.* **14**, 4618 (2023).

43. T. Pietzsch, S. Saalfeld, S. Preibisch, P. Tomancak, BigDataViewer: visualization and processing for large image data sets. *Nat. Methods* **12**, 481–483 (2015).

44. A. Subramanian, P. Tamayo, V. K. Mootha, S. Mukherjee, B. L. Ebert, M. A. Gillette, A. Paulovich, S. L. Pomeroy, T. R. Golub, E. S. Lander, J. P. Mesirov, Gene set enrichment analysis: a knowledge-based approach for interpreting genome-wide expression profiles. *Proc. Natl. Acad. Sci. U. S. A.* **102**, 15545–15550 (2005).

45. A. Liberzon, A. Subramanian, R. Pinchback, H. Thorvaldsdóttir, P. Tamayo, J. P. Mesirov, Molecular signatures database (MSigDB) 3.0. *Bioinformatics* **27**, 1739–1740 (2011).

46. S. Fishilevich, R. Nudel, N. Rappaport, R. Hadar, I. Plaschkes, T. Iny Stein, N. Rosen, A. Kohn, M. Twik, M. Safran, D. Lancet, D. Cohen, GeneHancer: genome-wide integration of enhancers and target genes in GeneCards. *Database (Oxford)* **2017**, bax028 (2017).

47. N. Sachs, J. de Ligt, O. Kopper, E. Gogola, G. Bounova, F. Weeber, A. V. Balgobind, K. Wind, A. Gracanin, H. Begthel, J. Korving, R. van Boxtel, A. A. Duarte, D. Lelieveld, A. van Hoeck, R. F. Ernst, F. Blokzijl, I. J. Nijman, M. Hoogstraat, M. van de Ven, D. A. Egan, V. Zinzalla, J. Moll, S. F. Boj, E. E. Voest, L. Wessels, P. J. van Diest, S. Rottenberg, R. G. J. Vries, E. Cuppen, H. Clevers, A living biobank of breast cancer organoids captures disease heterogeneity. *Cell* **172**, 373–386.e10 (2018).

Supplementary Information:

Table1
Annotation for untargeted MALDI phenotyping

Table2
Gene list for lipid CRISPR library